Supporting Information

Reconstructed porous copper surface promotes high selectivity and efficiency toward C_2 products by electrocatalytic CO_2 reduction

Jianyu Han, Chang Long, Jing Zhang, Ke Hou, Yi Yuan, Dawei Wang, Xiaofei Zhang, Xueying Qiu, Yanfei Zhu, Yin Zhang, Zhongjie Yang, Shuhao Yan, Zhiyong Tang*

Chemicals. All chemicals, solvents and materials were used as received without any further purification. Polycrystalline copper foil (0.5 mm, 99.9999%), potassium iodide (99%) and phosphoric acid were purchased from Alfa Aesar. Potassium hydrogen carbonate ($KHCO_3$, 99.99%) was bought from Macklin. Carbon dioxide (CO_2, 99.999%) and nitrogen (N_2, 99.9999%) were supplied by Beijing Beiwen Gases Company. Ultrapure water (Millipore Milli-Q grade) used in all experiments was with a resistivity of 18.2 MΩ.

Fabrication of Re-Cu-I. An aqueous solution containing 6 mM KI and 0.1 M $KHCO_3$ was used as electrolyte. A polycrystalline Cu foil (0.5×2.5 cm^2) was firstly electropolished in phosphoric acid (85 wt% aqueous solution) at 3 V *vs.* a Ti wire electrode for 12 min in a two-electrode system. The electropolished Cu foil was then flushed with ultrapure water and dried with N_2 gun. Subsequently, the obtained Cu foil electrode was submerged in the above electrolyte for electrochemical cycling and reconstructing of the surface morphology. The cyclic voltammetry (CV) was conducted at potential ranging from -0.59 V to 0.91 V *vs.* RHE at scan rate of 5 mV/s for 6 cycles using an Ag/AgCl (3.5 M KCl) as reference electrode and a platinum mesh as counter electrode. After that, the cooper electrode surface was flushed with ultrapure water and dried with flowing N_2 gas and stored in glovebox for characterization and electrocatalytic measurement.

Re-Cu-Br and Re-Cu-Cl were prepared by similar method except that 6 mM KI was changed to 6 mM KBr or 6 mM KCl, respectively.

Electrochemical measurements. All the electrochemical CO_2 measurements were carried out using a CHI 660E potentiostat in three-electrode configuration using gauze platinum electrode as a counter electrode and Ag/AgCl (3.5 M KCl) as a reference electrode, respectively. Potentials measured were converted to reversible hydrogen electrode (RHE) reference scale by E (*vs.* RHE) = E (*vs.* Ag/AgCl) + 0.210 + 0.059 × pH.

Electrochemical CO_2 reduction was conducted in a gas-tight two-component electrochemical cell separated by Nafion 117 cation-exchange membrane. A 0.1 M $KHCO_3$ (pH 6.8) aqueous solution was used as electrolyte and was purged with CO_2 (99.999%) at the speed of 30 mL/min for at least 30 minutes prior to electrolysis. During the electrolysis, the electrolyte at the cathodic part was under continuously mild stir and bubbled with CO_2 at the speed of 8 mL/min. The evolved gas products were conveyed into gas-sampling loop of a gas chromatograph (GC, Shimadzu GC-2014C) equipped with a packed Molecular Sieve 5A capillary column (Agilent) and a Porapak Q column (Agilent, 80-100 mesh). Both thermal conductivity detector (TCD) and flame ionization detector (FID) were installed on the GC to detect the evolved gas products. The liquid products were determined by ^{1}HNMR (Bruker Advance 400 spectrometer, 400 MHz) via water suppression using a presaturation method. A 0.9 mL of electrolyte was mixed with 0.1 mL of D_2O, and 2.0 ppm dimethyl sulfoxide (DMSO) was added as the internal standard.

The Faradaic efficiency (FE) was calculated from the concentration determined by GC using the following equitation:

$$\mathrm{FE}\ \% = \mathrm{ppm} \times \text{flow rate} \times (\mathrm{nFp_0/RT}) \times (j_{\mathrm{Tot}})^{-1} \times 100$$

where ppm was the concentration of gas determined by GC, the flow rate of outlet gas was determined by the soap film flowmeter, n was the electron transfer number, F was the Faradaic constant, p_0 was the pressure, T = 273.15 K and j_{Tot} was the total current density.

The half-cell power conversion efficiency (PCE) was calculated by the following equitation:

$$\mathrm{PCE} = \Sigma\ (1.23 + (-\mathrm{E}_{\mathrm{C}2(\mathrm{products})})) \times \mathrm{FE}_{\mathrm{C}_2} / (1.23+(-\mathrm{E}))$$

where $\mathrm{E}_{\mathrm{C}2(\mathrm{products})}$ was the thermodynamic potential (*vs*. RHE) of corresponding C_2 species, $\mathrm{FE}_{\mathrm{C}_2}$ was the determined FE of corresponding C_2 species, and E was the applied potential *vs*. RHE.

A two electrode system using gauze platinum electrode as a counter electrode was used for full-cell PCE calculation. The full-cell PCE without iR compensation was calculated by the following equation:

$$\mathrm{PCE} = \Sigma\ (1.23 + (-\mathrm{E}_{\mathrm{C}2(\mathrm{products})})) \times \mathrm{FE}_{\mathrm{C}2}\ /\text{applied voltage}$$

where the applied voltage was the potential applied at the current density in the two-electrode system.

Cyclic voltammetry (CV) was collected using the same setup as described above in 0.1 M $KHCO_3$. The working electrode compartment was purged with N_2 or CO_2 for 30 minutes. CV scans were collected in the range of -1.2 to 0.9 V *vs.* RHE at a scan rate of 20 mV/s.

During the long-term electrolysis, a graphite electrode was employed as the counter electrode to prevent possible etching from the conventional transition metal anode. The electrolyte was aged with Chelex (a solid supported iminodicactate) followed by pre-electrolyzing at a constant current density of 20 $\mu A/cm^2$ with two titanium electrodes in a two electrode system. These two methods were utilized to minimize the side effect of contaminants during the reaction. Furthermore, CO2 is continuously fed into $KHCO_3$ solution during the whole electrolysis process in order to guarantee the enough supply.

Characterization. Scanning electron microscopy (SEM) and elemental mapping were conducted on a Hitachi S4800 field emission scanning electron microscope (FESEM) equipped with an energy dispersive X-ray spectroscopy (EDS). A Rigaku D/MAX-TTRIII (CBO) X-ray power diffractometer was used to get powder X-ray diffraction (PXRD) patterns by using Cu Kα radiation (λ = 1.5418 Å). X-ray photoelectron was carried out on a Thermal-Fisher X-ray photoelectron (ESCALAB250Xi). The Co L-edge X-ray absorption spectra were acquired in vacuum at beamline 4B7B of the Beijing Synchrotron Radiation Facility (BSRF), using a variable-included-angle Monk-Gillieson mounting monochromator with a varied-line-spacing plane.

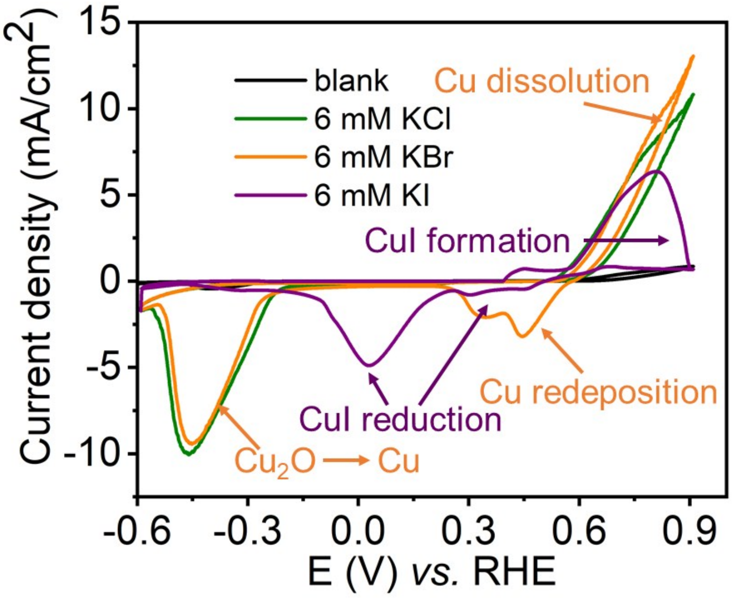

Fig. S1 Cyclic voltammetry (CV) curves of redox cycling of Cu electrodes in 0.1 M $KHCO_3$ aqueous solution in the presence of 6 mM KCl, KBr and KI.

In the CV curve in the presence of KI, the oxidation wave at potential from 0.4 V to 0.9 V is assigned to the dissolution and formation of insoluble CuI (purple curve). Note that a dramatically decread current denisty appears at 0.9 V *vs*. RHE, which is caused by passivation of the Cu electrode surface with as-formed insoluble CuI. The reduction wave at potential ranging from 0.3 V to -0.15 V is ascribed to reduction of CuI to form metallic Cu.

$$2CuCl + H_2O \rightarrow Cu_2O + 2H^+ + 2Cl^- \qquad (S1)$$

In the CV curves in the presence of KCl or KBr, the linearly increased current at potential from 0.6 V to 0.9 V is assigned to continuous Cu dissolution (green and organge). The reduction wave at potential ranging from 0.6 V to 0.3 V is ascribed to Cu redeposition and formation of Cu_2O. As shown in equation S1, the CuCl also can undergo rapid hydrolysis to form the Cu_2O in the aqueous solution according to the Pourbaix diagram. Since CuCl is more soluble in the aqueous solution, it is more easily converted to Cu_2O through this competitive non-electrochemical process in the aqueous solution compared with CuBr. Therefore, the reduction wave ranging from -0.35 V to -0.6 V in the presence of KCl is not as significant as that with addition of KBr. This phenomenon is also observed in the literature[1]. The reduction wave at potentials from -0.35 V to -0.6 V is attributed to reduction of Cu_2O to form metallic Cu.

At the oxidizing potential ranging from 0.4 V to 0.9 V, the addition of halides anions (X^-) promotes the corrosion of metallic Cu to form CuX. Thus, the oxidation current is much higher in the presence of X^- than that with $KHCO_3$ alone..

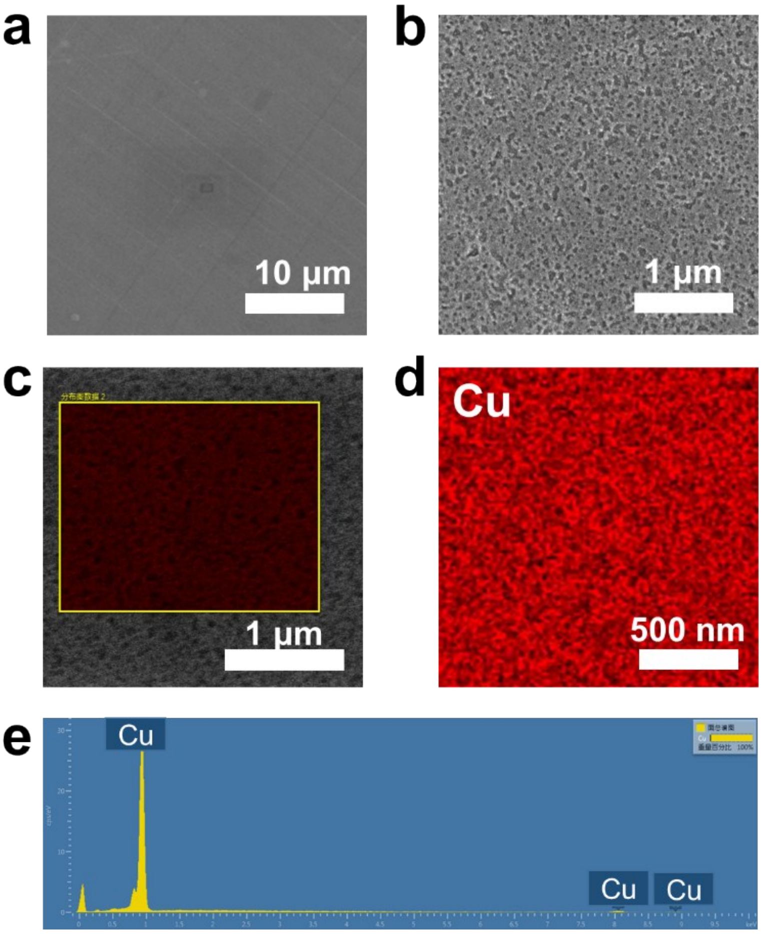

Fig S2. (a,b) SEM images of EP-Cu. (c,d,e) SEM-EDS elemental mapping results of EP-Cu.

The elemental mapping results suggest that the EP-Cu is in the Cu^0 state.

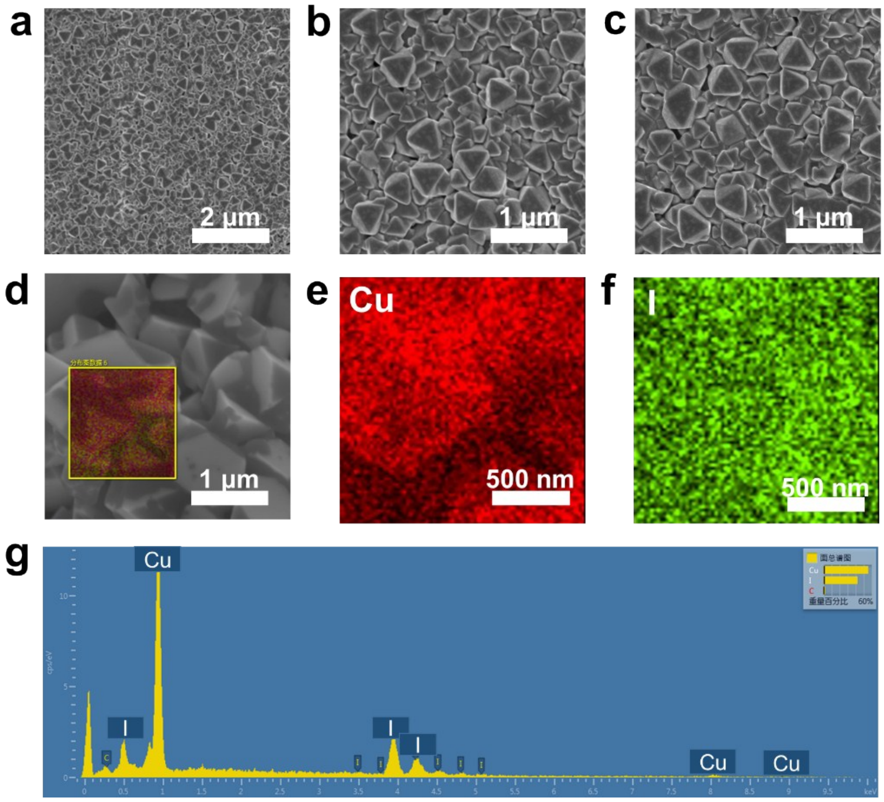

Fig S3 (a-c) SEM images of Ox-Cu. (d-g) SEM-EDS elemental mapping results of Ox-Cu.

The elemental mapping results suggest that the oxidized Cu in the polyhedral Ox-Cu is in the form of CuI.

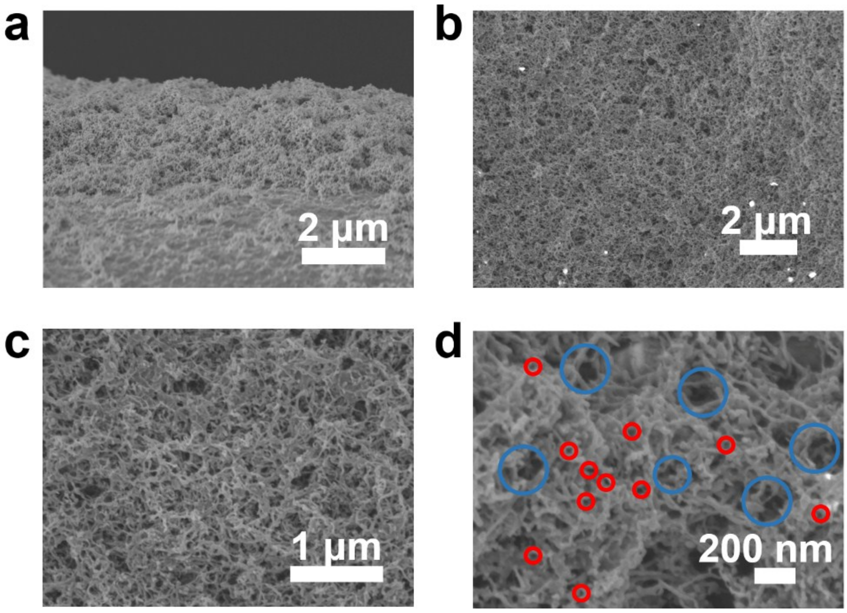

Fig. S4 Cross-sectional SEM images (a) and surface SEM images (b-d) of Re-Cu-I.

The densely packed nanowires are observed to interconnect with each other to form a three-dimensional network. The gaps between the interconnected nanowires result in the formation of pores of various size ranging from mesopores (< 50 nm, maked with red circles) to macrospores (> 50 nm, marked with blue circles).

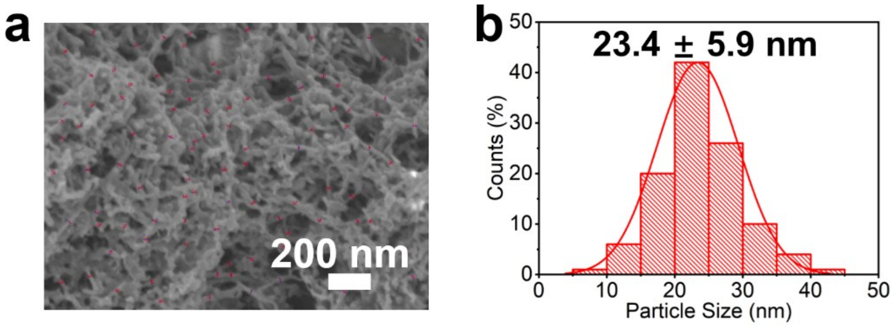

Fig. S5. (a) SEM image of Re-Cu-I. (b) The diameter distribution and calculated average diameter of nanowires in Re-Cu-I.

One hundred samples are counted by the “Nano measurer” software to measure the average diameters of the nanowires (Fig. S5a). The statistical diameter is of 23.4 ± 5.9 nm.

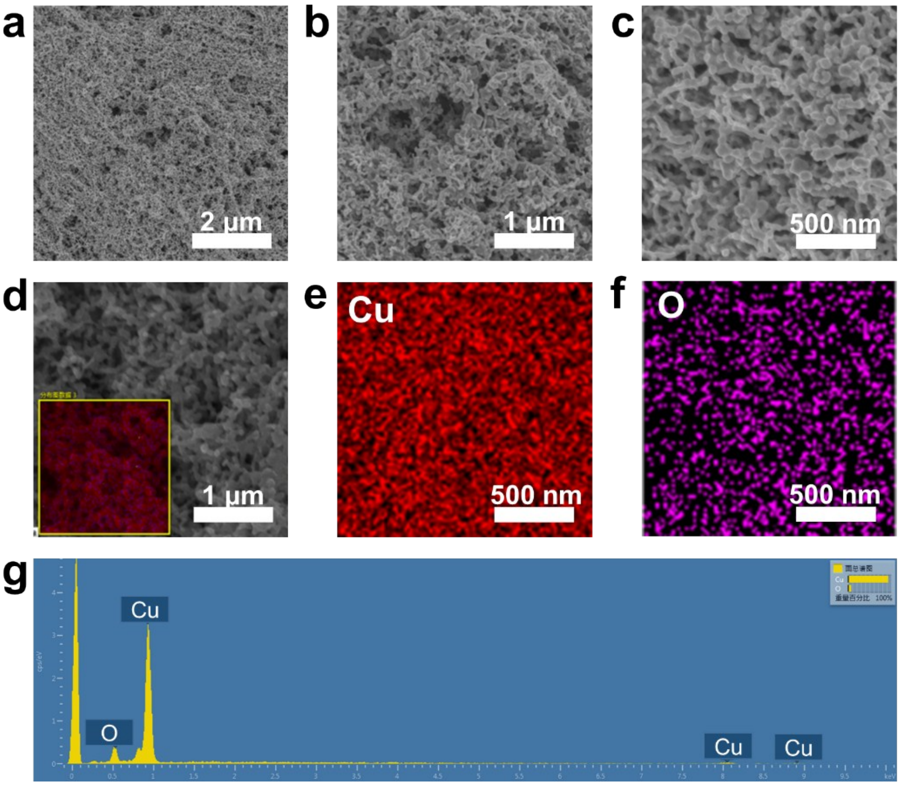

Fig S6 (a-c) SEM images of Re-Cu-I. (d-g) SEM-EDS elemental mapping results of Re-Cu-I.

A porous structure composed of entangled Cu nanowires is synthesized on the Cu electrode surface after oxidation-reduction cycling in the presence of I^-. Only Cu and O are determined by the EDS elemental mapping with molar percentage of 88.2% and 10.8% (Table S1).

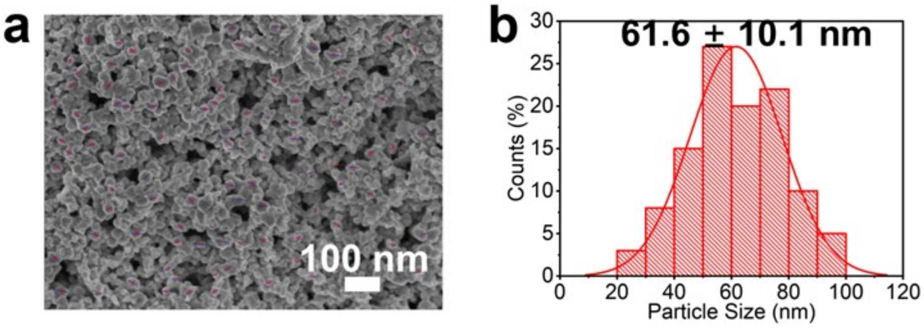

Fig. S7. (a) SEM image of Re-Cu-Br. (b) The diameter distribution and calculated average diameter of nanocubes in Re-Cu-Br.

After the reductive potential is applied, rather dense structure consisted of quasi-cubic nanoparticles of diameters in 61.6 ± 10.1 nm is produced on the surface of Re-Cu-Br.

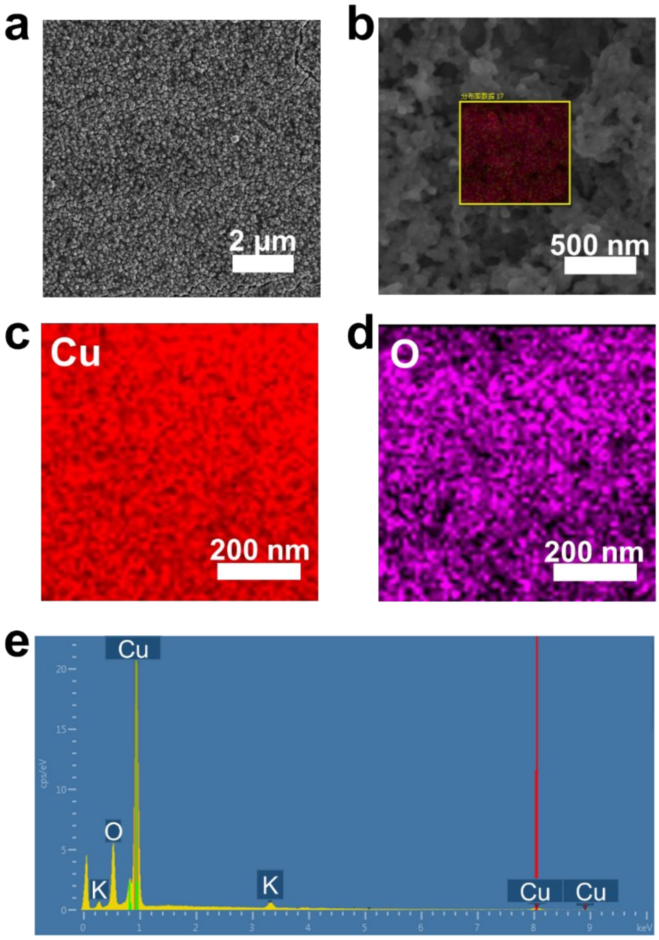

Fig S8 (a) SEM images of Re-Cu-Br. (b-e) SEM-EDS elemental mapping results of Re-Cu-Br.

Cu nanoparticles are obtained after surface reconstruction of Cu electrode in the presence of KBr. Cu and O are determined by the EDS elemental mapping with molar percentage of 82.6% and 17.4% (Table S1).

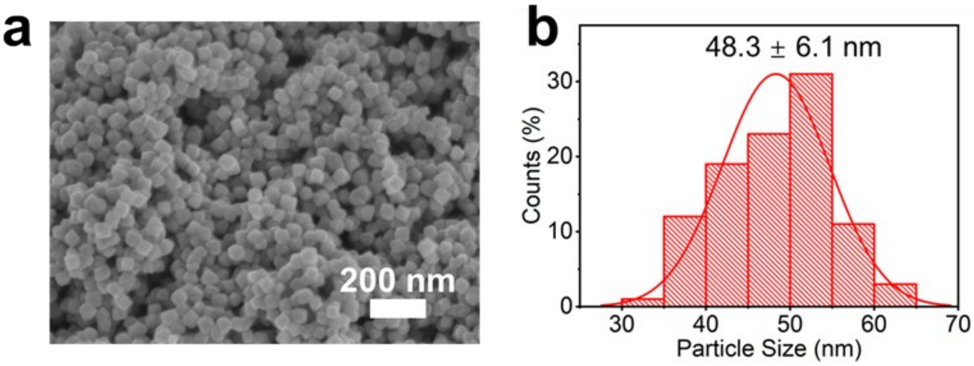

Fig. S9. (a) SEM image of Re-Cu-Cl. (b) The diameter distribution and calculated average diameter of nanocubes in Re-Cu-Cl.

After the reductive potential is applied, rather dense structure consisted of cubic nanoparticles of diameters in 48.3 ± 6.1 nm is produced on the surface of Re-Cu-Cl.

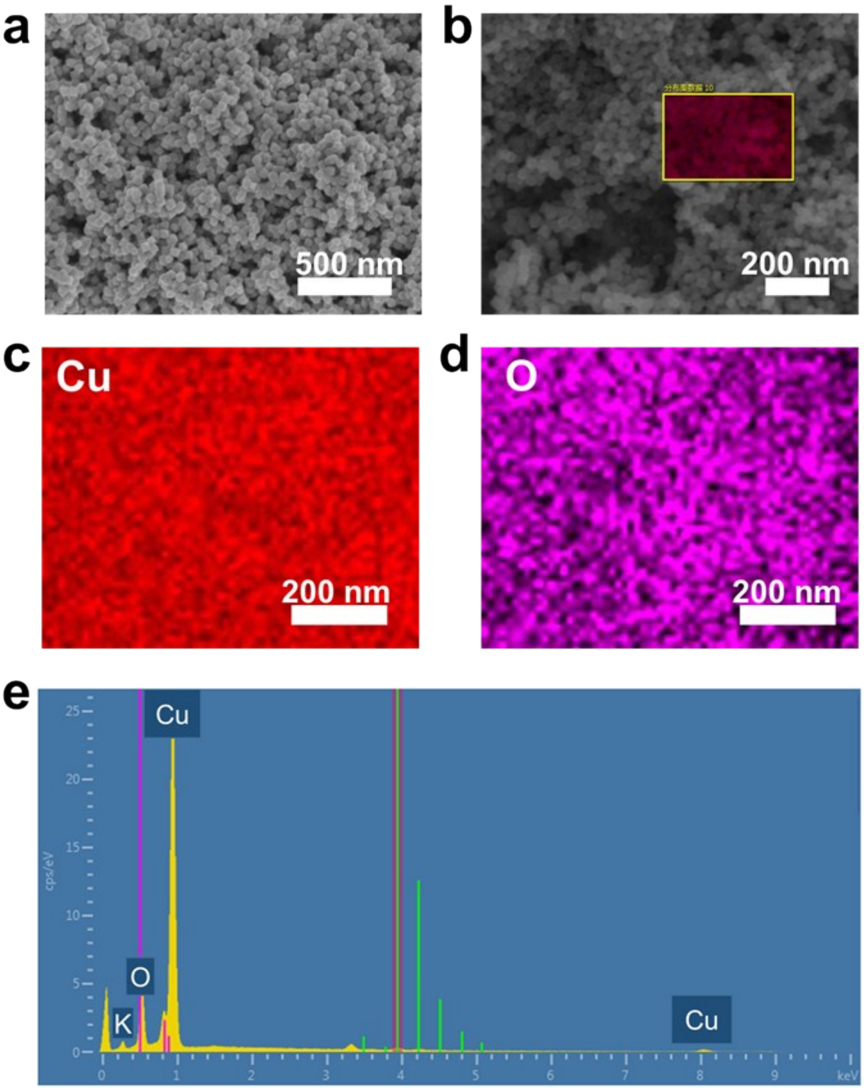

Fig S10 (a) SEM images of Re-Cu-Cl. (b-e) SEM-EDS elemental mapping results of Re-Cu-Cl.

Cu nanocubes are obtained after surface reconstruction of Cu electrode in the presence of KCl. Cu and O are determined by the EDS elemental mapping with molar percentage of 83.5% and 16.5% (Table S1).

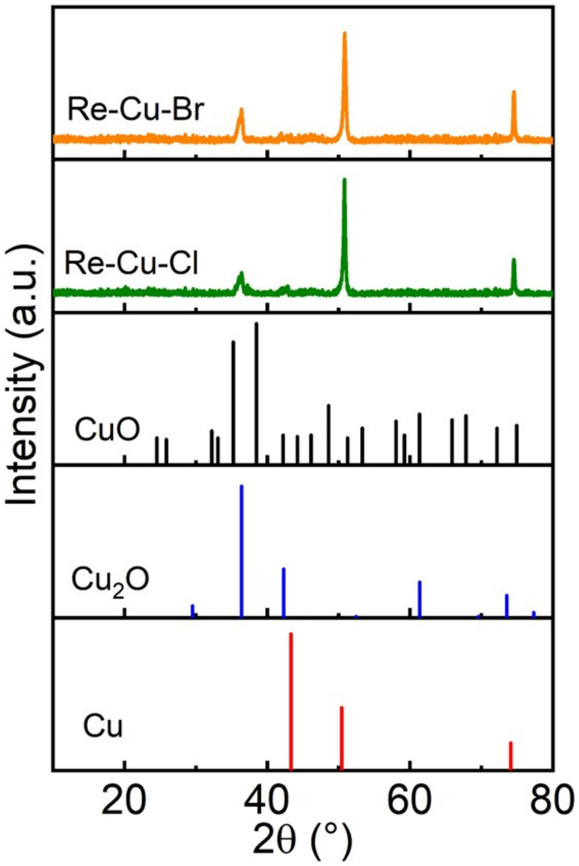

Fig. S11 GIXRD patterns of Re-Cu-Br (organge), Re-Cu-Cl (green), and reference samples CuO (black PDF#44-0706), Cu_2O (blue, PDF#05-0667), Cu (red, PDF#04-0836).

The XRD patterns show that the major phase in the Re-Cu-Br and Re-Cu-Cl are also metallic Cu accompanied with minor Cu_2O. The Cu (200) is the dominant facet in the Re-Cu-Br and Re-Cu-Cl.

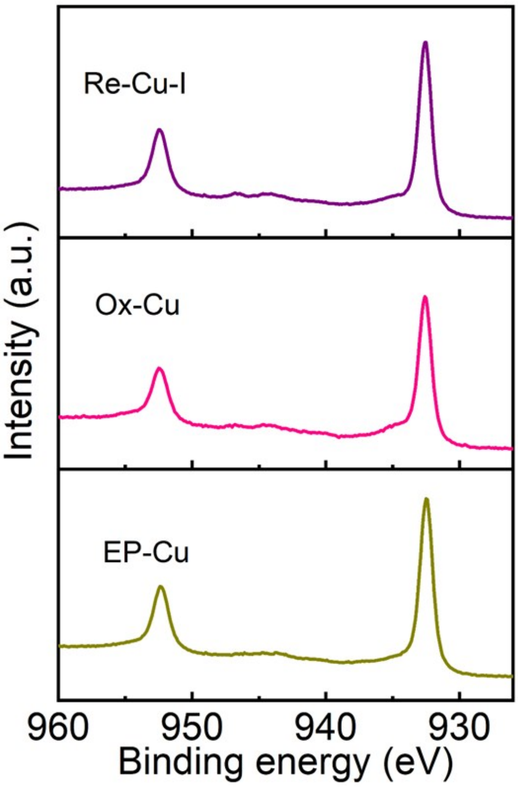

Fig. S12 Cu 2p XPS spectra of EP-Cu, Ox-Cu and Re-Cu-I.

A strong peak at 932.4 eV in the Cu $2p_{3/2}$ is found for EP-Cu, Ox-Cu and Re-Cu-I, which is ascribed to Cu^0 or Cu^+. The absence of satellite peak excludes the existence of Cu^{2+} species.

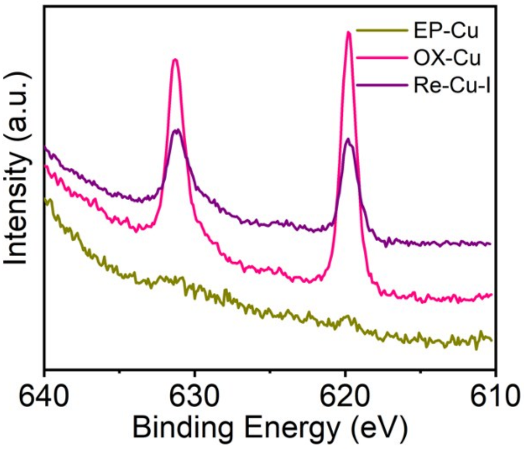

Fig. S13 I 2p XPS spectra of EP-Cu, Ox-Cu and Re-Cu-I.

The strong I 2p peak at 619 eV is discerned in Ox-Cu, further confirming formation of CuI in the oxidized state. The reduced (but not eliminated) signal of I 2p peak in Re-Cu-I should come from I^- adsorbed on the surface of Cu electrode.

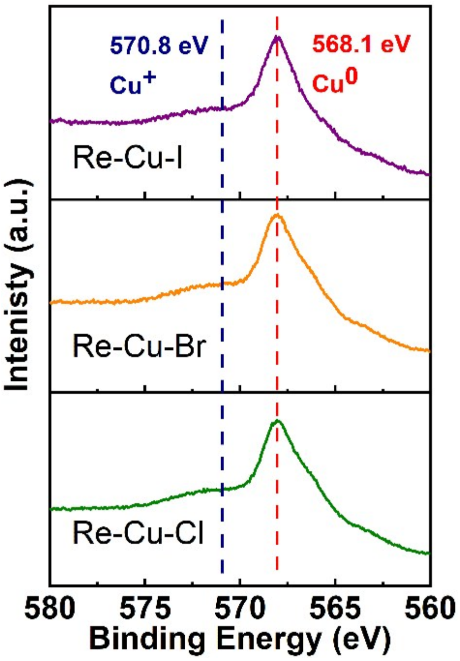

Fig. S14 Cu LMM spectra of Re-Cu-I (purple), Re-Cu-Br (orange) and Re-Cu-Cl (green).

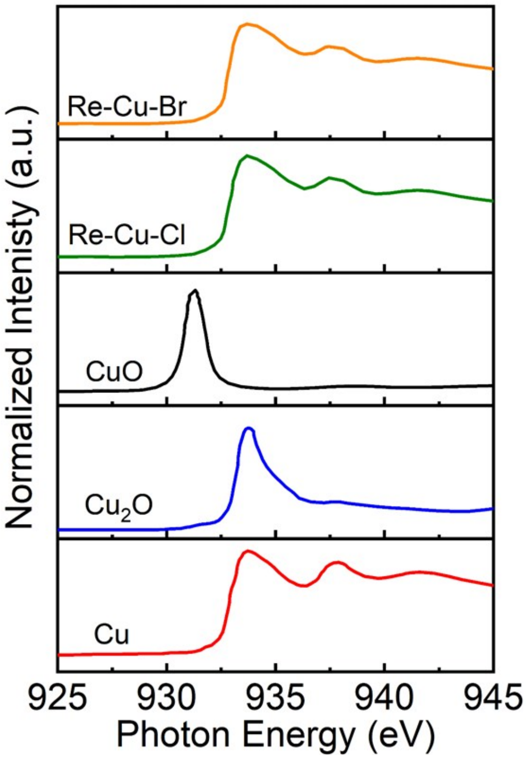

Fig. S15 Cu L-edge XAS spectra of Re-Cu-Br (oragne), Re-Cu-Cl (green) and reference samples CuO (black), Cu$_2$O (blue) and Cu (red).

The concentrations of Cu^0 determined in Re-Cu-Br and Re-Cu-Cl is 63% and 67% respectively, where the rest Cu species in these two samples are Cu$^+$ species (Table S2).

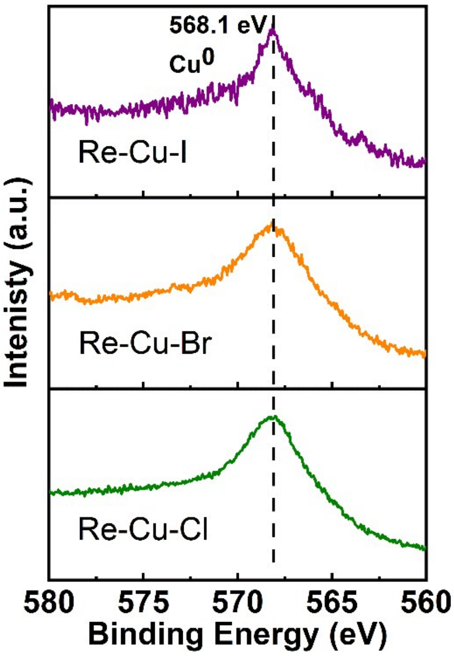

Fig. S16 Cu LMM spectra of Re-Cu-I (purple), Re-Cu-Br (orange) and Re-Cu-Cl (green) after pre-electrolysis at -0.99 V vs. RHE for 15 min.

Only one strong peak at 568.1 eV is observed for Re-Cu-I, Re-Cu-Br and Re-Cu-Cl verifying that all the three electrodes after pre-electrolysis are composed of metallic Cu.

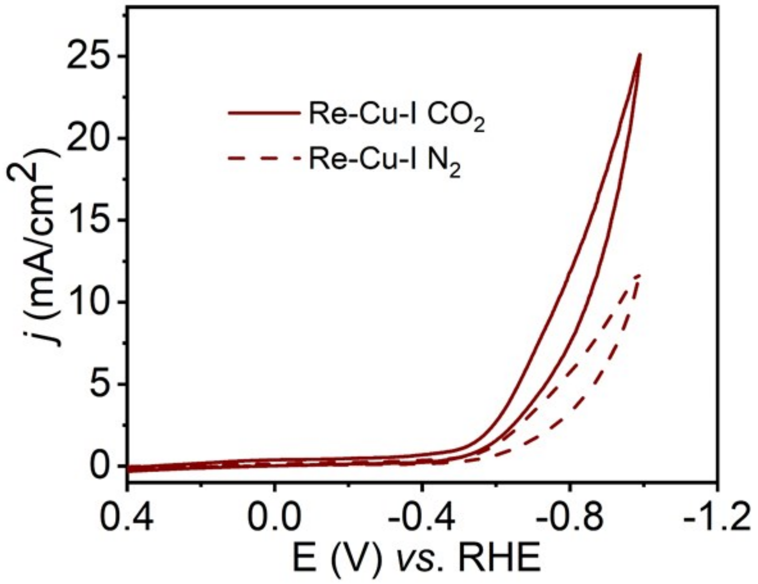

Fig. S17 CVcurves of Re-Cu-I in 0.1 M $KHCO_3$ saturated with N_2 or CO_2 at 20 mV/s.

The current density under CO_2 atmosphere is two orders of magnitude higher than that under N_2 atmosphere, implying that the Re-Cu-I is an excellent catalyst toward CO_2 reduction.

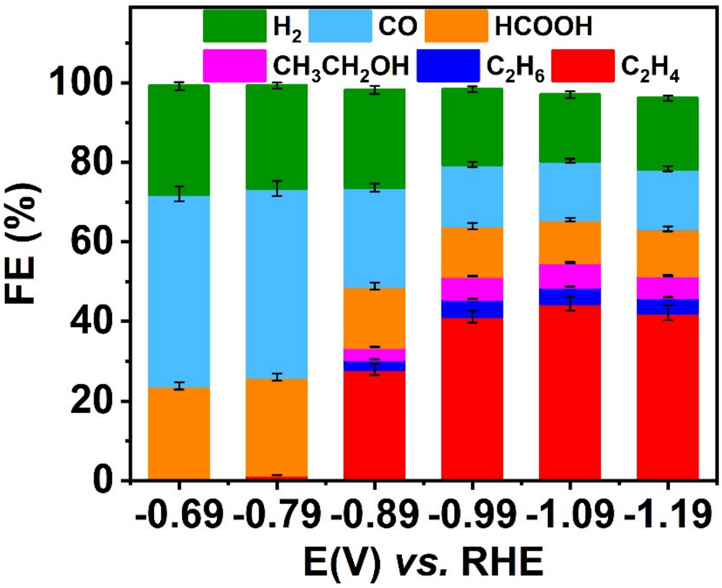

Fig. S18 FE of carbon products on Re-Cu-Br at potential ranging from -0.69 V to -1.19 V *vs.* RHE.

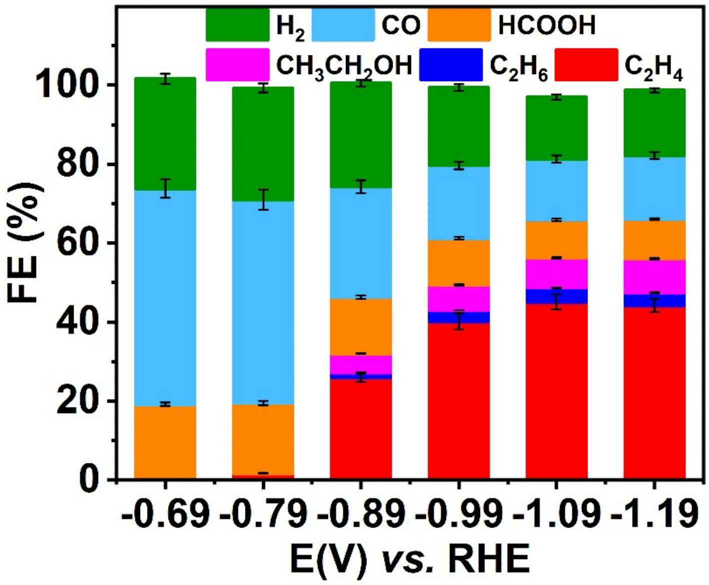

Fig. S19 FE of carbon products on Re-Cu-Cl at potential ranging from -0.69 V to -1.19 V *vs.* RHE.

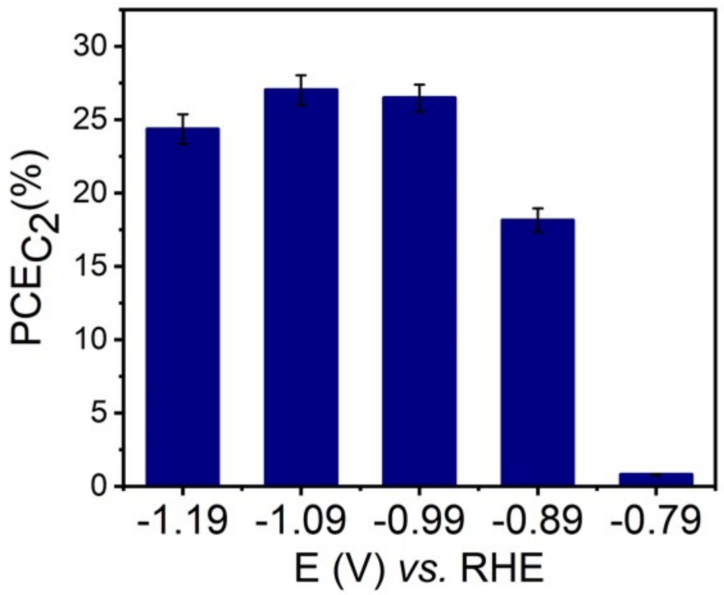

Fig. S20 PCE of C_2 products on Re-Cu-Br at potential ranging from -0.79 V to -1.19 V *vs.* RHE.

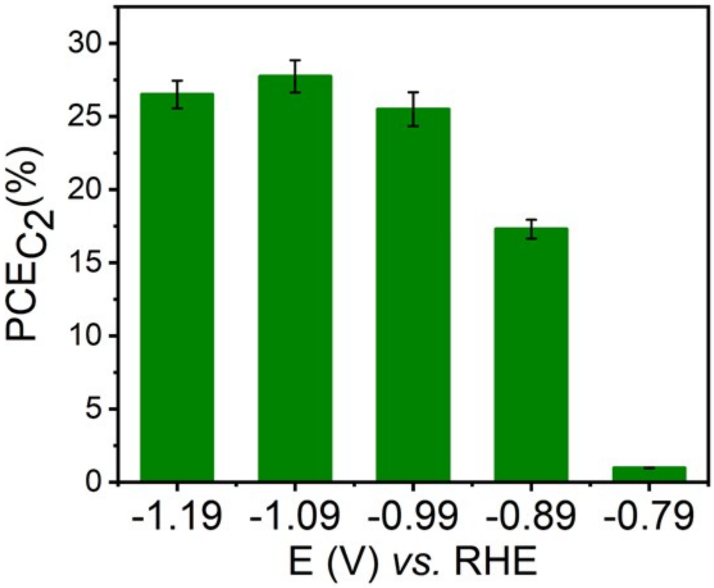

Fig. S21 PCE of C_2 products on Re-Cu-Cl at potential ranging from -0.79 V to -1.19 V *vs.* RHE.

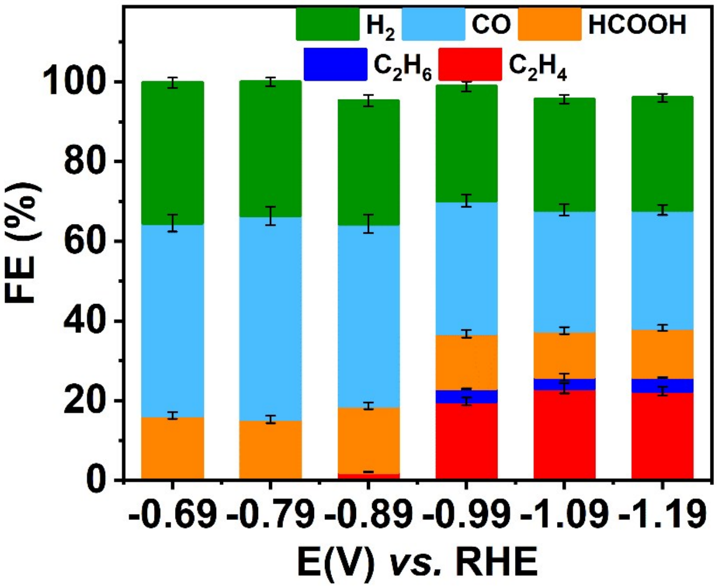

Fig. S22 FE of carbon products on EP-Cu at potential ranging from -0.69 V to -1.19 V *vs.* RHE.

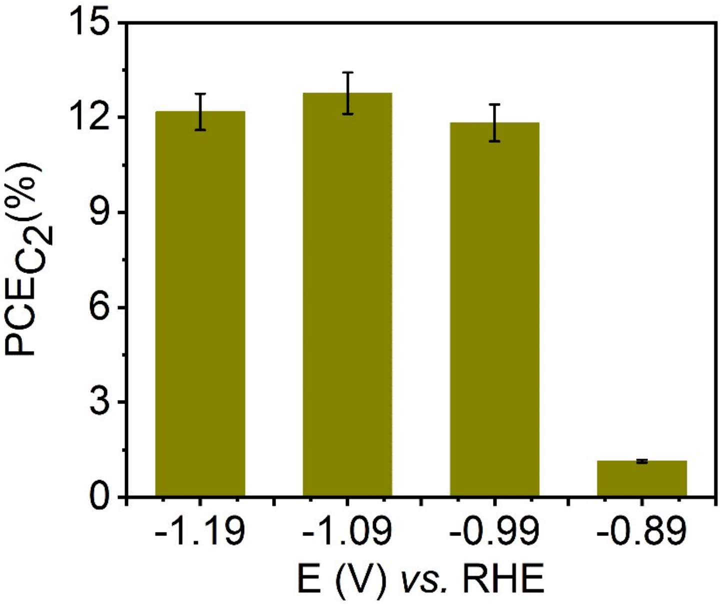

Fig. S23 PCE of C_2 products on EP-Cu at potential ranging from -0.89 V to -1.19 V *vs.* RHE.

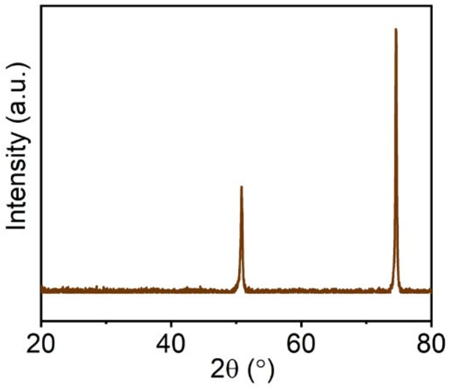

Fig. S24 GIXRD patterns of Re-Cu-I after electrochemical CO_2 reduction.

The in-plane XRD pattern of Re-Cu-I after the electrochemical CO_2 reduction only exhibits Cu (200) and Cu (220) facets, suggesting that oxidized Cu^+ is reduced during electrocatalytic CO_2 reduction.

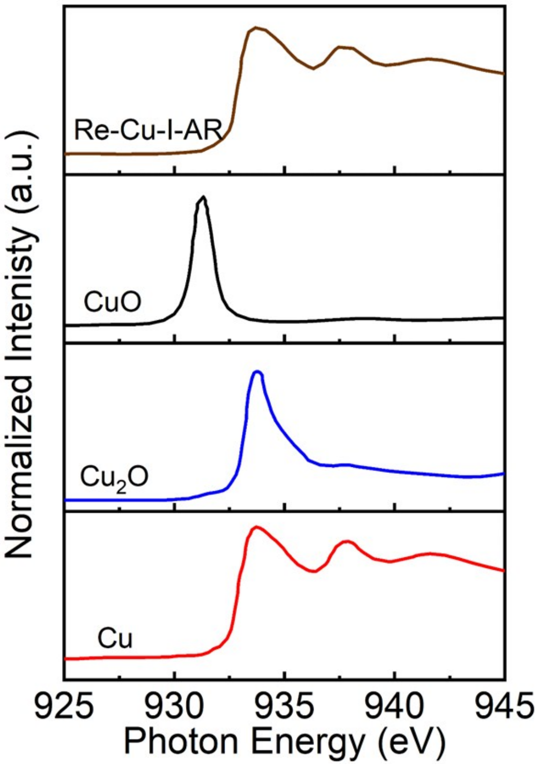

Fig. S25 Cu L-edge XAS spectra of Re-Cu-I after electrochemical CO_2 reduction and reference samples CuO (black), Cu_2O (blue) and Cu (red).

Fitting of Cu L-edge XAS spectrum of Re-Cu-I after the reaction shows that the electrode contains 96% Cu^0 and 4% Cu^+ (Table S2). The residual Cu^+ should be attributed to rapid oxidation after removal of reduction potential.

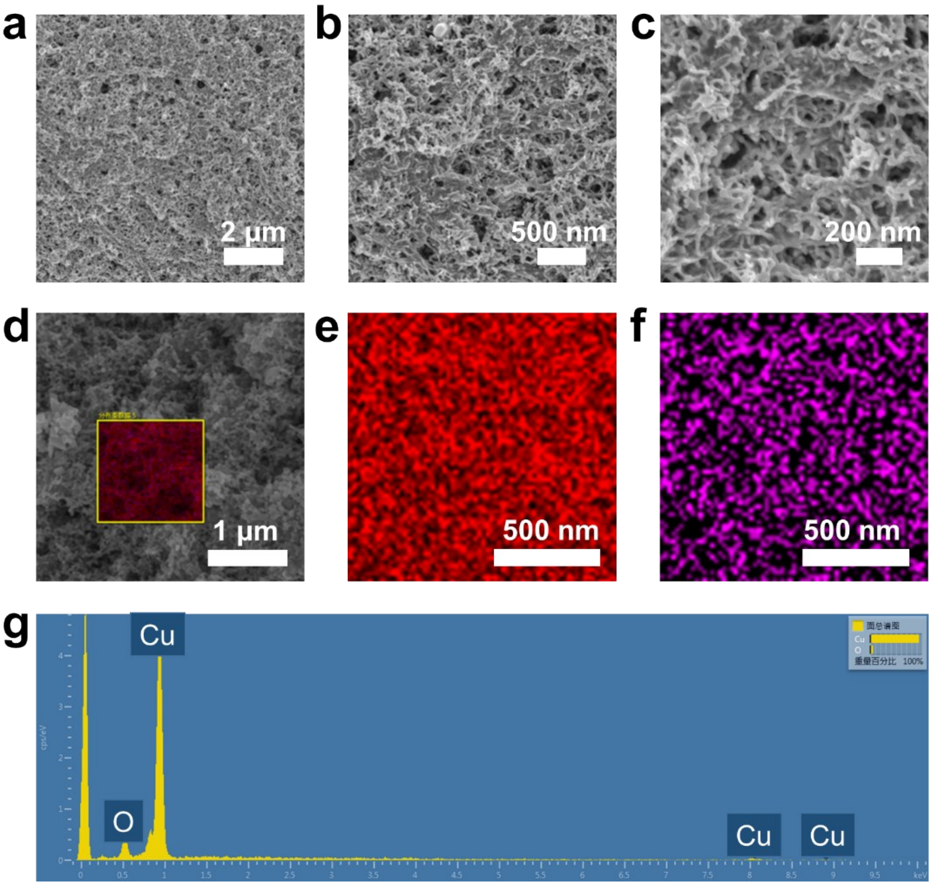

Fig. S26 (a-c) SEM images of Re-Cu-I after reaction. (d-g) SEM-EDS elemental mapping results of Re-Cu-I after reaction.

Negligible morphology change is observed for the Re-Cu-I after the reaction as evidenced by SEM images. The trace amount of O detected by EDS is consistent with the XAS result, which comes from rapid oxidation after removal of reduction potential.

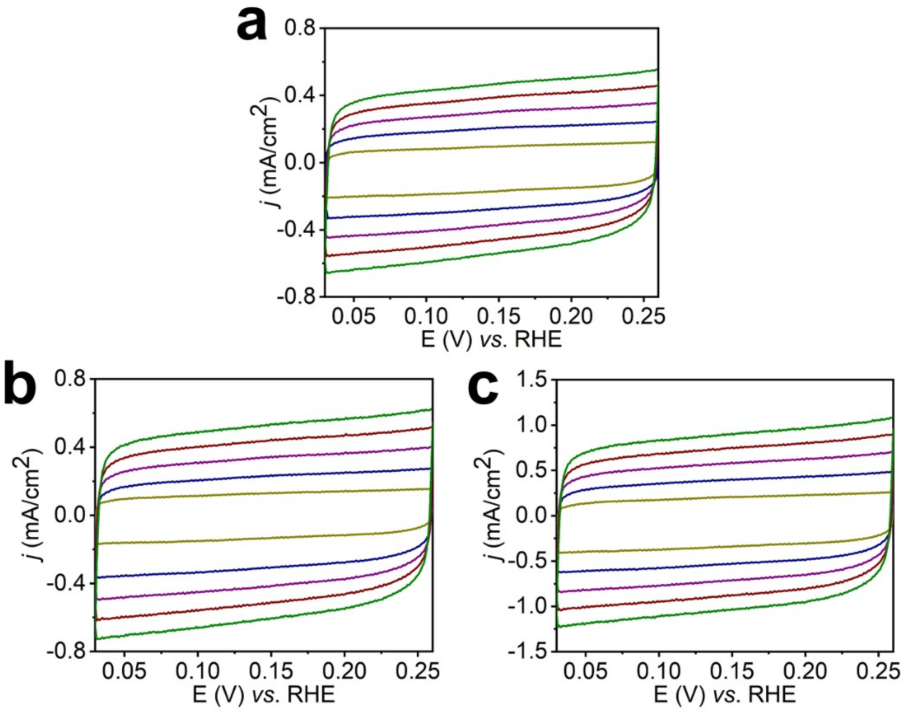

Fig. S27 CVs of Re-Cu-I, Re-Cu-Br and Re-Cu-Cl taken at a range of scan rates in potential window from 0.03 V to 0.26 V *vs.* RHE, where only double-layer capacitance is relevant.

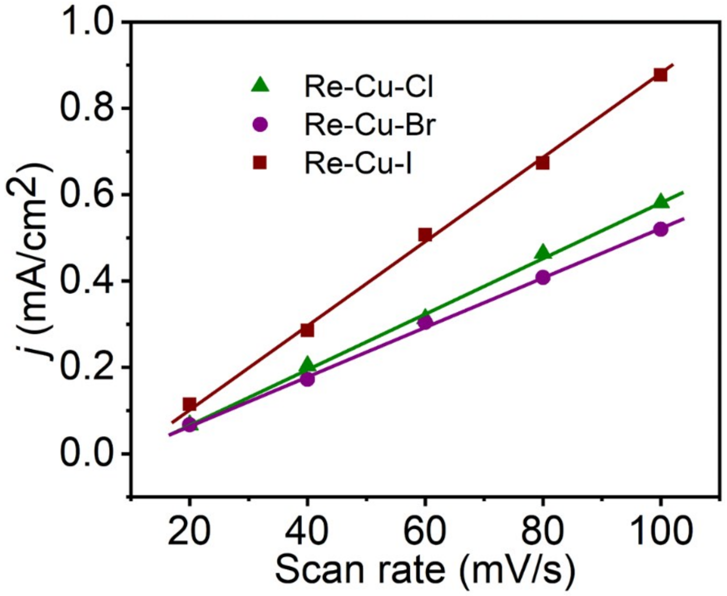

Fig. S28 Current density in double-layer capacitance region plotted against CV scan rate.

The capacitance values of Re-Cu-I, Re-Cu-Br and Re-Cu-Cl are calculated to be 7.6 mF, 4.5 mF and 5.4 mF, respectively, by fitting the plots of current density *vs.* scan rate. The corresponding surface roughness factor (RF) is then determined to be 262, 154 and 186, respectively.

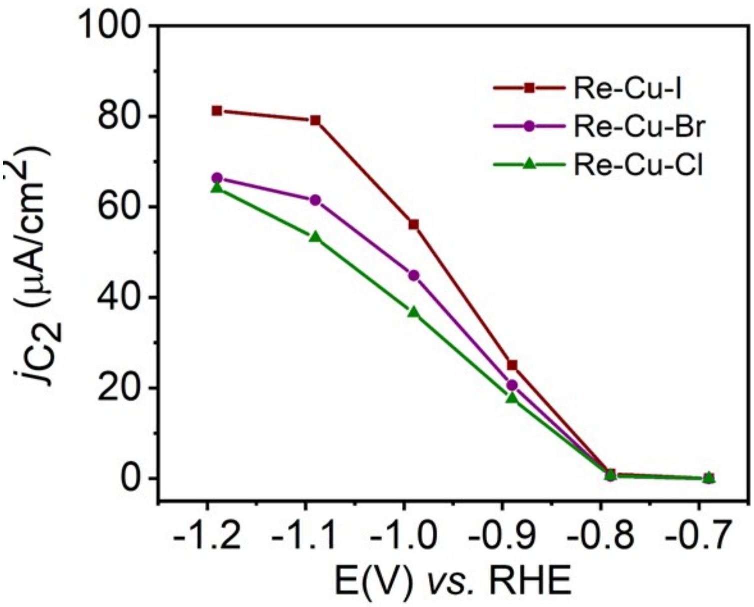

Fig. S29 ECSA normalized C_2 partial current density of Re-Cu-I, Re-Cu-Br and Re-Cu-Cl at potential from -0.69 V to -1.19V *vs.* RHE.

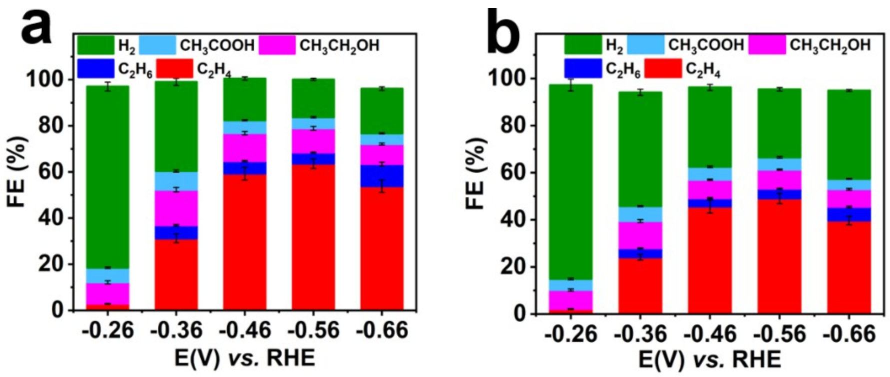

Fig. S30 FE of carbon products from CO electroreduction on Re-Cu-I with CO flow rate of 4 mL/min (a) and 2 mL/min (b) at potential ranging from -0.26 V to -0.66 V *vs.* RHE.

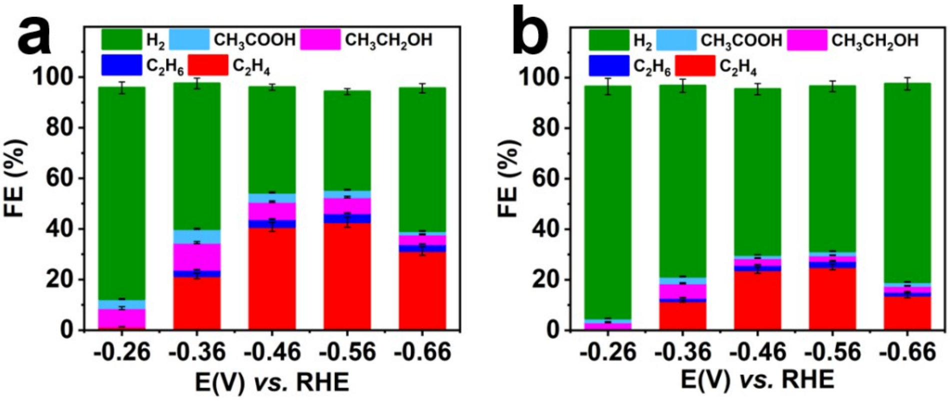

Fig. S31 FE of carbon products from CO electroreduction on Re-Cu-Cl with CO flow rate of 4 mL/min (a) and 2 mL/min (b) at potential ranging from -0.26 V to -0.66 V *vs.* RHE.

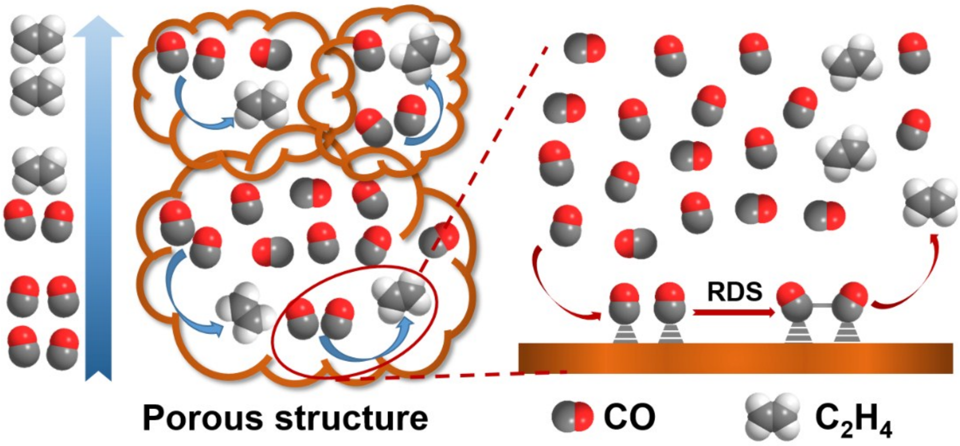

Fig. S32 Schematic illustration of enrichment effect of porous structure for enhanced C_2 production.

Table S1. Summary of element percentage in EP-Cu, Ox-Cu, Re-Cu-I, Re-Cu-Br and Re-Cu-Cl obtained by EDS elemental mapping.

	Cu	**O**	**I**
EP-Cu	100%	-	-
Ox-Cu	72.7%	-	27.3%
Re-Cu-I	88.2%	11.8%	-
Re-Cu-Br	82.6%	17.4%	-
Re-Cu-Cl	83.5%	16.5%	-

Table S2. Summary of percentage of Cu^0, Cu^+ and Cu^{2+} obtained by linear fitting of Cu L-edge XAS in EP-Cu, Re-Cu-I, Re-Cu-Br, Re-Cu-Cl, and Re-Cu-I after electrocatalytic reaction.

	$\mathbf{Cu^0}$	$\mathbf{Cu^+}$	$\mathbf{Cu^{2+}}$
EP-Cu	100%	-	-
Re-Cu-I	75%	25%	-
Re-Cu-Br	63%	37%	-
Re-Cu-Cl	67%	33%	-
Re-Cu-I after reaction	96%	4%	-

Table S3. Comparison of percentage of Cu^0, Cu^+ in EP-Cu, Re-Cu-I, Re-Cu-Br, and Re-Cu-Cl obtained by XAS technique and EDS method.

	XAS		**EDS**	
	Cu^0	Cu^+	Cu^0	Cu^+
EP-Cu	100%	-	100%	
Re-Cu-I	75%	25%	74%	26%
Re-Cu-Br	63%	37%	59%	41%
Re-Cu-Cl	67%	33%	62%	38%

Table S4. Comparison of electrocatalytic CO_2 reduction performance on Re-Cu-I with the literature reported values.

Catalyst	**Reaction conditions**	**j_{C2+} (mA/cm^2)**	**FE$_{C2+}$ (%)**	**PCE$_{C2+}$ (%)**	**Reference**
Re-Cu-I	0.1 M $KHCO_3$[a]	21	80	39	this work
Cu CIPH	7 M KOH[b]	1300	65-75	45	Reference[2]
Cu-CO_2-60	7 M KOH[b]	520	90	37	Reference[3]
Cu-12	1 M $KHCO_3$[b]	230	72	20	Reference[4]
Branched Cu	0.1 M $KHCO_3$[a]	17	70	35	Reference[5]
Cu(B)-2	0.1 M $KHCO_3$[a] 0.1 M KCl	50	79	38	Reference[6]
Reconstructed Cu	3 M KOH[b]	336	84	50	Reference[7]
Cu/PTFE	7 M KOH[b]	210	84	53	Reference[8]
Cu nanodendrites	1 M $KHCO_3$[b] 0.1 M KBr	97	57	28	Reference[9]
CuDAT-wire	1 M $KHCO_3$[b]	114	60	32.5	Reference[10]
N doped graphene QDs	1 M KOH[b]	40	67	36	Reference[11]
Plasma Cu nanocubes	0.1 M $KHCO_3$[a]	36	73	36	Reference[12]
Plasma OD Cu	0.1 M $KHCO_3$[a]	12	60	33	Reference[13]

a. The electrocatalytic CO_2 reduction reaction is performed in H-type cell.

b. The electrocatalytic CO_2 reduction reaction is performed in flow cell.

The full-cell PCE without iR compensation at the current density of 21 mA/cm^2 is calculated to be 28%, which is lower than the half-cell PCE due to voltage loss across the cell.

Reference

1. Y. Kwon, Y. Lum, E. L. Clark, J. W. Ager and A. T. Bell, *ChemElectroChem*, 2016, **3**, 1012-1019.
2. F. P. García de Arquer, C.-T. Dinh, A. Ozden, J. Wicks, C. McCallum, A. R. Kirmani, D.-H. Nam, C. Gabardo, A. Seifitokaldani, X. Wang, Y. C. Li, F. Li, J. Edwards, L. J. Richter, S. J. Thorpe, D. Sinton and E. H. Sargent, *Science*, 2020, **367**, 661-666.
3. Y. Wang, Z. Wang, C.-T. Dinh, J. Li, A. Ozden, M. Golam Kibria, A. Seifitokaldani, C.-S. Tan, C. M. Gabardo, M. Luo, H. Zhou, F. Li, Y. Lum, C. McCallum, Y. Xu, M. Liu, A. Proppe, A. Johnston, P. Todorovic, T.-T. Zhuang, D. Sinton, S. O. Kelley and E. H. Sargent, *Nat. Catal.*, 2020, **3**, 98-106.
4. F. Li, A. Thevenon, A. Rosas-Hernandez, Z. Wang, Y. Li, C. M. Gabardo, A. Ozden, C. T. Dinh, J. Li, Y. Wang, J. P. Edwards, Y. Xu, C. McCallum, L. Tao, Z. Q. Liang, M. Luo, X. Wang, H. Li, C. P. O'Brien, C. S. Tan, D. H. Nam, R. Quintero-Bermudez, T. T. Zhuang, Y. C. Li, Z. Han, R. D. Britt, D. Sinton, T. Agapie, J. C. Peters and E. H. Sargent, *Nature*, 2020, **577**, 509-513.
5. J. Kim, W. Choi, J. W. Park, C. Kim, M. Kim and H. Song, *J. Am. Chem. Soc.*, 2019, **141**, 6986-6994.
6. Y. Zhou, F. Che, M. Liu, C. Zou, Z. Liang, P. De Luna, H. Yuan, J. Li, Z. Wang, H. Xie, H. Li, P. Chen, E. Bladt, R. Quintero-Bermudez, T. K. Sham, S. Bals, J. Hofkens, D. Sinton, G. Chen and E. H. Sargent, *Nat. Chem.*, 2018, **10**, 974-980.
7. M. G. Kibria, C. T. Dinh, A. Seifitokaldani, P. De Luna, T. Burdyny, R. Quintero-Bermudez, M. B. Ross, O. S. Bushuyev, F. P. Garcia de Arquer, P. Yang, D. Sinton and E. H. Sargent, *Adv. Mater.*, 2018, **30**, 1804867.
8. C.-T. Dinh, T. Burdyny, M. G. Kibria, A. Seifitokaldani, C. M. Gabardo, F. P. García de Arquer, A. Kiani, J. P. Edwards, P. De Luna, O. S. Bushuyev, C. Zou, R. Quintero-Bermudez, Y. Pang, D. Sinton and E. H. Sargent, *Science*, 2018, **360**, 783-787.
9. C. Reller, R. Krause, E. Volkova, B. Schmid, S. Neubauer, A. Rucki, M. Schuster and G. Schmid, *Adv. Energy. Mater.*, 2017, **7**, 1602114.
10. T. T. H. Hoang, S. Ma, J. I. Gold, P. J. A. Kenis and A. A. Gewirth, *ACS Catal.*, 2017, **7**, 3313-3321.
11. J. Wu, S. Ma, J. Sun, J. I. Gold, C. Tiwary, B. Kim, L. Zhu, N. Chopra, I. N. Odeh, R. Vajtai, A. Z. Yu, R. Luo, J. Lou, G. Ding, P. J. A. Kenis and P. M. Ajayan, *Nat. Commun.*, 2016, **7**, 13869.
12. D. Gao, I. Zegkinoglou, N. J. Divins, F. Scholten, I. Sinev, P. Grosse and B. Roldan Cuenya, *ACS Nano*, 2017, **11**, 4825-4831.
13. H. Mistry, A. S. Varela, C. S. Bonifacio, I. Zegkinoglou, I. Sinev, Y. W. Choi, K. Kisslinger, E. A. Stach, J. C. Yang, P. Strasser and B. R. Cuenya, *Nat. Commun.*, 2016, **7**, 12123.